Massive Star Formation at the Periphery of the Evolved Giant H II Region W 39

C. R. Kerton

Department of Physics & Astronomy, Iowa State University, Ames, IA 50011, USA

kerton@iastate.edu

K. Arvidsson

Astronomy Department, Adler Planetarium, 1300 S. Lake Shore Drive, Chicago, IL 60605, USA

karvidsson@adlerplanetarium.org

and

M. J. Alexander

Department of Physics & Astronomy, University of Wyoming, 1000 E. University, Laramie, WY 82071, USA

malexan9@uwyo.edu

Received _____; accepted _____

January 14, 2013; Accepted for Publication in the Astronomical Journal

ABSTRACT

We present the first detailed study of the large, $\sim$ 30 pc diameter, inner-Galaxy H II region W 39. Radio recombination line observations combined with H I absorption spectra and Galactic rotation models show that the region lies at $V_{\rm LSR} = +65.4 \pm 0.5$ km s^{-1} corresponding to a near kinematic distance of 4.5$\pm$0.2 kpc. Analysis of radio continuum emission shows that the H II region is being powered by a cluster of OB stars with a combined hydrogen-ionizing luminosity of $\log(Q) \geq 50$, and that there are three compact H II regions located on the periphery of W 39, each with $\log(Q) \sim 48.5$ (single O7 - O9 V star equivalent). In the infrared, W 39 has a hierarchical bubble morphology, and is a likely site of sequential star formation involving massive stars. Kinematic models of the expansion of W 39 yield timescales of order Myr consistent with a scenario where the formation of the smaller H II regions has been triggered by the expansion of W 39. Using *Spitzer* GLIMPSE and MIPSGAL data we show that star-formation activity is not distributed uniformly around the periphery of W 39 but is concentrated in two areas that include the compact H II regions as well as a number of intermediate-mass Class I and Class II YSOs.

Subject headings: H II regions – stars: formation – stars: pre-main-sequence

1. Introduction

W 39 is a large H II region in the inner Galaxy ($l = 19°$, $b = -0.^{\circ}4$) first identified in the Westerhout (1958) 1.4 GHz radio continuum survey and more recently cataloged as a large infrared "bubble" by both professional astronomers (N24; Churchwell et al. 2006) and citizen scientists (MWP1G18908-003146; Simpson et al. 2012). It is a significant high-mass star-forming region and a possible example of sequential or triggered star formation based on the hierarchical bubble structure seen in the infrared, but, owing to its highly obscured location in the inner Galaxy, it has been poorly studied. Recent high-resolution (sub-arcminute) surveys at radio and infrared wavelengths have provided an opportunity to examine this region in detail for the first time. This paper presents an analysis of the H II region itself along with an investigation of the influence of the H II region on star formation in its vicinity.

In the next section the key parameters of the various data sets used in the study are summarized. The determination of the radial velocity and distance to the H II region is described in §3. An analysis of W 39 and three associated compact H II regions follows in §4. In §5 the young stellar object (YSO) distribution surrounding W 39 is explored, and our conclusions are presented in §6.

2. Observations

2.1. Radio Line & Continuum

At cm radio wavelengths we use VLA Galactic Plane Survey (VGPS; Stil et al. 2006) 21-cm line and continuum data. The VGPS maps have an angular resolution of ~ 1 arcmin, and the H I line spectra have a velocity resolution of 1.56 km s^{-1}. The maps include single-dish short-spacing data, making them ideal for obtaining flux density measurements

of large angular scale ($\gtrsim$ 30 arcmin) objects like W 39.

To trace molecular gas we use ^{13}CO (J=1−0) observations from the Boston University/Five College Radio Astronomy Observatory Galactic Ring Survey (BU/FCRAO GRS; Jackson et al. 2006). These data have an angular resolution of 46 arcsec and 0.21 km s^{-1} velocity resolution. We also make use of 1.1 mm continuum data from the Bolocam Galactic Plane Survey (BGPS; Rosolowsky et al. 2010).

2.2. Infrared

At infrared wavelengths we primarily use data from the GLIMPSE (Benjamin et al. 2003) *Spitzer* legacy survey. GLIMPSE provides 1.7 to 2.0 arcsec resolution images in four bands centered at 3.6, 4.5, 5.8, and 8.0 μm along with a point source catalog that contains near- and mid-infrared photometric data. In addition, we use the 6 arcsec resolution images at 24 μm from the MIPSGAL *Spitzer* legacy survey (Carey et al. 2009). For near-infrared photometry of point sources we use data from the Two-Micron All Sky Survey (2MASS; Skrutskie et al. 2006) and the United Kingdom Infrared Telescope (UKIRT) Infrared Deep Sky Surveys-Galactic Plane Survey (UKIDSS-GPS; Lucas et al. 2008).

3. Radial Velocity and Distance

3.1. Radial Velocity

In Figure 1 we show the VGPS 1420 MHz continuum map of the area around W 39 along with the position and velocity of cm-wavelength observations of the radio recombination lines (RRL) H85α, H87α, and H88α (Lockman 1989). W 39 has a bubble morphology best seen in the infrared. At radio wavelengths the brightest emission ($\geq$ 50 K)

from W 39 is concentrated along a U-shaped ridge opening to lower Galactic longitudes. Fainter emission ($\sim$ 30 – 40 K) is found within the bubble and also tracing the bubble edges at lower Galactic longitude. There is a local minimum in the radio emission around $l = 19\overset{\circ}{.}025, b = -0\overset{\circ}{.}38$ that is a likely location for the exciting OB star(s). Three of the RRL observations that lie on the strong ridge of emission have very similar velocities, and we adopt the average of these values, $V_{\rm LSR} = 65.4 \pm 0.5$ km s^{-1}, as the radial velocity of W 39. The RRL velocity of G18.95-0.02 is significantly different from the main ridge and, as we discuss in §3.1.2, this region is likely not directly associated with W 39.

The nature of the RRL emission associated with the arc-shaped structure G18.64-0.29 is more speculative. Both Helfand et al. (2006) and Brogan et al. (2006) classify this object as a supernova remnant (SNR) based on multi-frequency radio observations, and H I absorption studies by Johanson & Kerton (2009) place the object at a distance of $\sim$ 5 kpc. RRL emission is not expected from SNRs so it is likely that the observed RRL emission, with a difference in velocity of only $\sim$ 5 km s^{-1} from the main W 39 ridge, is originating from the edge of the W 39 bubble.

3.1.1. HI Absorption

H I absorption spectra, obtained from the VGPS, were used to determine if all three of the RRL sources are located at the same near or far kinematic distance. A radio continuum source in the inner Galaxy at the near distance can only show absorption up to its $V_{\rm LSR}$ while a source at the far distance can show absorption at velocities beyond $V_{\rm LSR}$ up to the tangent velocity, which at $l \sim 19^\circ$ is 110 to 140 km s^{-1} depending on the kinematic model used (see § 3.2).

For each of the RRL sources H I "ON" spectra were obtained by averaging H I spectra

where the 1420 MHz continuum brightness temperature was above a threshold of 100 K for G19.07-0.28, 100 K for G18.88-0.49, and 55 K for G19.04-0.43. "OFF" spectra were then calculated by taking the average H I spectrum of a nearby (1–2 arcmin offset) similarly sized region. The resulting ON-OFF absorption spectra are shown in Figure 2.

The uncertainty in an absorption spectrum $\sigma_{\rm abs}$ can be quantified by taking the maximum of either the standard deviation in channels where no absorption is expected to occur (e.g., at negative $V_{\rm LSR}$ in this case) or by constructing "OFF-OFF" spectra that measure the intrinsic variability of H I emission structure. We found $\sigma_{\rm abs} \sim 5$ K in each case. Looking at Figure 2 we see that the two brightest RRL sources are clearly at the near kinematic distance because of the lack of absorption at velocities $\gtrsim 65$ km s^{-1}. The ridge RRL source has a much poorer quality spectrum, but there is no evidence for absorption beyond ~ 65 km s^{-1}. We conclude that all of the emission associated with the three RRL observations is at the near kinematic distance.

3.1.2. IR Morphology

In Figure 3 we show an 8 and 24 μm image of the W 39 region using data from *Spitzer* GLIMPSE and MIPSGAL. The infrared bubble structure, best seen at 8 μm and identified by Churchwell et al. (2006) and Simpson et al. (2012), is indicated by an ellipse. As expected for a thermal radio source W 39 is very bright in the infrared. Of particular interest though is the layered structure of the infrared emission; moving from the interior of the U-shaped structure to the exterior, we first see 24 μm emission followed by a layer of 8 μm emission. This is exactly what would be expected for a region being heated from one side by ionizing radiation. Within the H II region polycyclic aromatic hydrocarbons (PAH) are strongly depleted allowing 24.0 μm emission from small dust grains to dominate while in the photodissociation region (PDR) surrounding the H II region PAHs can survive

resulting in strong 8 μm emission (e.g., Tielens et al. 1993; Giard et al. 1994; Kerton et al. 2008; Arvidsson & Kerton 2011). The continuity of this layered infrared morphology is consistant with W 39 being a single large H II region.

We note that this layered infrared morphology does not extend to the region around $l = 18\overset{\circ}{.}95, b = -0\overset{\circ}{.}01$. In Figure 4 we show GRS maps of ^{13}CO emission between $0 \leq V_{\rm LSR} \leq +130$ km s^{-1} integrated in 20 km s^{-1} increments between 0 and +40 km s^{-1}, 10 km s^{-1} increments between 40 and +70 km s^{-1}, and a single 60 km s^{-1} interval between +70 and +130 km s^{-1}. The G18.95-0.01 region is morphologically very similar to CO emission seen in the GRS at $V_{\rm LSR} \sim +45$ km s^{-1} consistent with the lower RRL velocity observed by Lockman (1989). Based on this we do not consider this region to be part of W 39. The CO maps also show that most of the molecular gas along the line of sight to W 39 is found between +60 and +70 km s^{-1}.

3.2. Kinematic Distance

The (near) kinematic distance to W 39 was calculated using $V_{\rm LSR} = 65.4 \pm 0.5$ km s^{-1} and three different Galactic rotation models: 1) the $R_\odot$= 8 kpc hydrodynamical model of Pohl et al. (2008), 2) the $R_\odot$=8.5 kpc, $V_\odot$=220 km s^{-1} model of Clemens (1985), and 3) a version of the Clemens (1985) model scaled to $R_\odot$=8.0 kpc. The resulting distances are 4.5 kpc, 4.7 kpc, and 4.4 kpc respectively. In each case the error in the calculated distance caused by the uncertainty in $V_{\rm LSR}$ is only $\sim$ 0.04 kpc, much less than the systematic uncertainty associated with the choice of rotation model. We adopt the average (standard deviation) of these values as the distance (uncertainty) to W 39: $d = 4.5 \pm 0.2$ kpc. At this distance, W 39 is probably part of the Scutum-Centaurus Arm of our Galaxy (Churchwell et al. 2009; Russeil 2003).

4. A Giant HII Region

4.1. Exciting Stars & Ionized Mass

The flux density at 1420 MHz of W 39, $F_{1420} = 40 \pm 0.6$ Jy, was measured from VGPS data using IMVIEW (Higgs et al. 1997) to integrate the emission within a user-defined area roughly following the $T_B = 30$ K contour, but omitting emission at $b > -0.^{\circ}1$ and subtracting the contribution from compact and point sources found within the contour. The main contribution to the uncertainty comes from the definition of the background level which varies depending on the number and location of the points used to define it and the order of the two-dimensional polynomial fit used.

The observed radio continuum flux density (F_ν) of an H II region at a distance (d) can be related to the ionizing radiation luminosity (Q) of the star(s) located within the H II region by:

$$\log\left(fQ\right) = 40.95 + \log\left(\frac{F_\nu}{\mathrm{Jy}}\right) + 2\log\left(\frac{d}{\mathrm{pc}}\right), \quad (1)$$

where f is the fraction of the ionizing radiation from the star(s) that is intercepted by the H II region (e.g., $f = 1$ for an ionization bounded region, $f \sim 0.5$ for a "blister" H II region), and we used $\nu = 1.4$ GHz and $T_e = 7500$ K to calculate the constant (Kerton et al. 1999; Matsakis et al. 1976). As pointed out by Rubin (1968) Equation 1 does not depend on the details of the density structure of the H II region.

For $d = 4500$ pc and $F_\nu = 40$ Jy we find $\log\left(fQ\right) = 49.86$, equivalent to the output of two O3 V stars (or 10 O7 V stars) using the calibration of Crowther (2005). Varying distance and F_ν within the uncertainties, and allowing T_e to range between 7500 K and 10,000 K, we find the full range of $\log\left(fQ\right) = 49.75 - 49.90$. Given the morphology of the H II region it is very likely that $f < 1$ and W 39 is a giant H II region (GHIIR; Conti & Crowther 2004) being powered by numerous OB stars.

The formulas given in Matsakis et al. (1976), and derived in detail in Mezger & Henderson (1967), can be used to estimate the average electron density of the H II region and the total mass of ionized gas given F_ν, d, T_e, and the angular size of the region. An appropriate size scale for W 39 is given by the separation between the two sides of the H II region, $\sim 0\overset{\circ}{.}4$, or 30 pc at 4.5 kpc. This is slightly smaller than the value of $0\overset{\circ}{.}6$ reported in Westerhout (1958), but that value included emission at higher Galactic latitude that we do not associate with the H II region. We find values of $n_e \sim 20$ cm^{-3} and $M \sim 10^4$ M$_\odot$. Unlike the $\log(fQ)$ calculation these values do depend strongly on the details of the H II region's density structure and should only be considered order-of-magnitude estimates.

4.2. G19.07-0.28 = IRAS 18239-1228

The radio source G19.07-0.28 is the brightest of the compact radio sources found on the periphery of W 39 with $F_\nu = 1.77 \pm 0.08$ Jy. Using the same formulas and calibrations from the previous subsection we find $\log(fQ) = 48.50$ equivalent to a single O8 V star. The ionized gas mass is $M \sim 50$ M$_\odot$ and the average electron density is $n_e \sim 160$ cm^{-3}. This radio source is also the infrared source IRAS 18239-1228 and has four well-defined IRAS flux density measurements. Using the technique of Emerson (1988) we calculate the far-infrared luminosity $\log(L_{\rm IR}/L_\odot) = 5.2 \pm 0.1$ which is the luminosity of an O7 - O8 V star.

The higher resolution GLIMPSE 8.0 μm image of the region is shown in Figure 5. At this wavelength the source is clearly a bubble structure with a radius of $\sim 0\overset{\circ}{.}01$ (~ 0.8 pc). Ionized gas, traced by the 1420 MHz radio emission, and warm dust, traced by 24 μm emission, fill the central region. The compact bubble morphology of the region and the agreement in the stellar spectral type determined by the radio and infrared flux support the idea that the region is ionization bounded ($f \sim 1$).

4.3. G18.88-0.49

The radio source G18.88-0.49 is the second brightest of the compact radio sources found on the periphery of W 39 with $F_\nu = 1.53 \pm 0.02$ Jy. From this we find $\log(fQ) = 48.45$ equivalent to a single O8 V star. The ionized gas mass is $M \sim 44$ $M_\odot$ and the average electron density is $n_e \sim 160$ cm^{-3}.

Unlike G19.07-0.28 there is no IRAS point source associated with this region. The higher resolution GLIMPSE 8.0 μm image of the region is shown in Figure 6. Although the morphology is more complex than G19.07-0.28, the presence of bright-rimmed structures at the edge of the radio continuum emission along with the coincident 24 μm emission suggest that we are also looking at a dusty, ionization-bounded, bubble structure similar in size to G19.07-0.28.

4.4. G18.94-0.43

The remaining radio source on the periphery of W 39 is G18.94-0.43. We measured $F_\nu = 0.8 \pm 0.09$ Jy, which corresponds to $\log(fQ) = 48.16$, equivalent to a single O9 V star. The ionized gas mass is $M \sim 32$ $M_\odot$, and the average electron density is $n_e \sim 110$ cm^{-3}.

As with G18.88-0.49 there is no IRAS point source associated with the region. The high resolution image of the region shown in Figure 6 reveals a complex morphology that is difficult to interpret in detail. As we would expect for an H II region there appears to be bright-rimmed structures along the low-latitude portion of the region and a minimum in the 8 μm emission coincident with the radio continuum maximum.

4.5. Timescales & Triggered Star Formation

The radio continuum view of the W 39 region is of an evolved massive HII region (powered by multiple mid- to early-type O stars) with multiple areas of less intense massive star formation (i.e., the three H II regions powered by single late O stars) occurring along the periphery of the region. One possibility is that these secondary regions of star formation have been triggered by the expansion of the W 39 H II region. While proving this idea is difficult we can at least investigate the relevant timescales for the most clearly defined secondary region, G19.07-0.28, to see if this scenario is at all plausible.

We can obtain a rough estimate of the age of G19.07-0.28 using the classic description of the evolution of an H II region (Spitzer 1978; Osterbrock 1989). The O star first creates a ionized gas region about the size of the Strömgren sphere on an essentially instantaneous timescale of $\sim 10^5/n_e(\mathrm{cm}^{-3})$ yr. The overpressurized H II region then expands from its initial radius, r_s to the observed radius R at time t as,

$$\frac{R}{r_s} = \left(1 + \frac{7C_{II}t}{4r_s}\right)^{4/7}, \tag{2}$$

where C_{II} is the isothermal sound speed in the ionized gas (~ 10 km s^{-1}).

To estimate the initial density of the cloud in which the H II region formed we examined the nearby 1.1 mm source from the BGPS, G019.077-00.287. The peak brightness of this source is 2.3 Jy beam^{-1} corresponding to a column density of $N_{H_2} = 7.9 \times 10^{22}$ cm^{-2} using equation A.27 in Kauffmann et al. (2008). The deconvolved radius of the source is 93.″82 (~ 2 pc). Adopting a path length of 4 pc we obtain a density $n \sim 10^{3.8}$ cm^{-3}. In such an environment an O8 V star would rapidly create an H II region of size $r_s \sim 0.2$ pc. Using this value and the observed size of the region ~ 0.8 pc in equation 2 we find $t \sim 10^5$ years.

While this is clearly a rough estimate it is important to note that this timescale is approximately one order of magnitude smaller than the timescales appropriate for the

evolution of the much larger W 39 region. As pointed out by Churchwell (1975), an approximate lower limit to the age of an evolved H II region can be obtained by the sound crossing time, $\sim 1.5 \times 10^6$ years in the case of W 39. The lack of non-thermal radio emission from SNRs gives a consistent upper limit to the age of $2 - 4 \times 10^6$ years based on the main sequence lifetime of early O stars (Schaerer & de Koter 1997). We conclude that the probable timescales associated with the expansion of W 39 ($\sim 10^6$ years) and the likely ages of the secondary regions of massive star formation ($\sim 10^5$ years) are consistent with a scenario of triggered star formation.

5. Star Formation Traced by MIPSGAL & GLIMPSE

5.1. GLIMPSE Detected YSO Candidates

In order to determine if the only recent, and thus likely triggered, star formation activity surrounding W 39 is restricted to the three compact H II regions discussed previously, we used the *Spitzer* GLIMPSE catalog to identify YSO candidates (YSOs hereafter) in the W 39 field within $18\overset{\circ}{.}5 < l < 19\overset{\circ}{.}3$, $-0\overset{\circ}{.}55 < b < -0\overset{\circ}{.}1$. The high latitude cutoff was chosen to avoid including the prominent infrared dark clouds (IRDCs) found at $b > -0\overset{\circ}{.}1$ which are not associated with W 39. A total of 10657 sources with valid magnitudes in all four IRAC bands were identified. Figure 7 is a color-color (CC) diagram showing all of these sources along with the YSO classification criteria from Allen et al. (2004). We identify 57 Class I YSOs, 129 Class II YSOs and 57 Class I/II YSOs ([3.6]-[4.5] < 0.4 and [5.8]-[8.0]> 1.1). Class I YSOs are objects with a substantial circumstellar envelope, Class II YSOs have most of the circumstellar material residing in a disk, and Class I/II objects are most likely Class II or stellar objects with poor [8.0] photometry causing them to scatter into this region of the CC diagram. In the canonical picture, a Class I YSO will evolve to a Class II YSO with each stage of evolution lasting for $\tau_I \sim 10^5$ years and $\tau_{II} \sim 10^6$ years respectively

(Ward-Thompson 2002).

In Figure 8 the sample is plotted in a [3.6]-[4.5] vs. [3.6] color-magnitude (CM) diagram. We see there is a bright cutoff at [3.6] ~ 7 due to saturation and a faint, color-dependent, sensitivity cutoff at [3.6] $\sim 13 - 15$. Included in the CM diagram are two lines showing the position of main-sequence stars (B0 V to M5 V) and giant stars (G5 III to M0 III) at a distance of 4.5 kpc. The crosses are T-Tauri stars from Hartmann et al. (2005) shifted from the distance of Taurus-Auriga to W 39. The diamonds are intermediate-mass Herbig AeBe stars from The et al. (1994) and Finkenzeller & Mundt (1984) again shifted to the distance of W 39. For the Herbig AeBe sample we have used L and M band magnitudes as rough proxies for [3.6] and [4.5]. Finally, the asterisks represent AGB stars from the *Spitzer*/IRAC study of Galactic AGB stars by Reiter, Marengo, & Fazio (in preparation). The CM diagram illustrates that our sample is primarily sensitive to intermediate-mass YSOs at a distance of 4.5 kpc. The CM diagram also provides some insights into likely contaminants in our sample. We see that the majority of background main-sequence stars are too faint to be detected while foreground main-sequence stars with moderate amounts of reddening will be a source of contamination for the least-red Class II YSOs. The major contaminant, for both Class I and Class II YSOs, are reddened background AGB stars. Unfortunately, since we are looking toward the inner Galaxy, background stellar distances approaching 20 to 30 kpc are possible meaning even the faintest, reddest, sources in our sample could be matched by a distant, heavily reddened AGB.

In Figure 9 we show the spatial distribution of the various YSO classes. It is clear that star formation activity is not uniformly distributed along the periphery of the W 39 bubble with the most striking feature being the lack of YSOs at the high and low longitude ends of the bubble around $b = -0.^{\circ}15$ and $b = -0.^{\circ}45$ respectively. This is consistent with the lack of molecular gas seen at these locations in the ^{13}CO images shown in Figure 4. There

is also a swath of YSOs located within the infrared bubble that roughly follows the ^{13}CO distribution seen in the lower left panel of Figure 4. Almost all of the ~ 10 Class I sources found within the bubble are associated with an IRDC that runs roughly from $l = 19\overset{\circ}{.}0$ to $l = 18\overset{\circ}{.}8$ at $b \sim -0\overset{\circ}{.}3$. If associated with W 39, these sources could represent recent star formation occurring in the near or far wall of the bubble, but it is also possible that the IRDC is not directly related to W 39. We tried to measure the $V_{\rm LSR}$ of the IRDC, but were unable to clearly identify any ^{13}CO features that were unambiguously associated with the IRDC. Higher resolution radio/mm line observations of this IRDC in tracers of cold, dense gas would help to clarify its relation to W 39.

Qualitatively it appears from Figure 9 that most of the star-formation activity located on the periphery of W 39 is concentrated around the compact H II regions. In order examine this quantitatively we divided our search area into 32 roughly $0\overset{\circ}{.}1 \times 0\overset{\circ}{.}1$ areas and calculated the percentage of sources in each area that have a YSO classification (see Figure 10). The "background" YSO percentage, using the median of the eight high and low longitude columns, is 1.8% with an interquartile range of 0.85%. The YSOs within the bubble show up as a slight excess over the background ($\sim 4\%$) but the main outliers are the areas around G18.88-0.49 and G19.07-0.28 with YSO percentages of 6.6% and 6.0% respectively.

5.2. MIPSGAL Detected YSOs around G18.88-0.49 and G19.07-0.28

We investigated the YSO population around G18.88-0.49 (19 YSOs; G18 hereafter) and G19.07-0.28 (17 YSOs; G19 hereafter) in more detail (the areas are shown in Figure 9). For each YSO, JHK photometry was obtained either from 2MASS or UKIDSS, and 24 μm photometry was obtained from MIPSGAL images if possible. UKIDSS photometry was used if an unambiguous match to the IRAC source could be made using a $0\overset{''}{.}6$ search radius,

otherwise the associated 2MASS photometry given in the GLIMPSE catalog was used. Aperture photometry on the MIPSGAL images was obtained for 15 of the YSOs using a 6 arcsec radius aperture, a user-defined aperture correction of 1.67, and a zero-magnitude flux density of 7.17 Jy (Engelbracht et al. 2007). We have adopted a conservative uncertainty of 10% for the [24] photometry due to image background variations and uncertainty in the aperture correction estimate. The YSO sample photometry is summarized in Table 1.

When available the 24 μm photometry provides a very clear discriminant between Class I and Class II YSOs. At or longward of 24 μm a Class II YSO's spectral energy distribution (SED) is typically flat or falling while a Class I YSO's SED will typically be rising. In Figure 11 we plot the sample of YSOs with 24 μm photometry on a [3.6]-[5.8] vs. [8.0]-[24] CC diagram along with the YSO classification criteria from Rho et al. (2006). As can be seen from comparing columns two and three of Table 2 the IRAC-only and IRAC & MIPS YSO classifications are typically in agreement. Two of the YSOs are classified in the Rho et al. (2006) scheme as possible "hot excess" sources, which are either very heavily embedded Class II YSOs or Class I YSOs undergoing very rapid accretion.

To confirm that our YSOs are most likely intermediate mass objects (i.e., $\sim 2-10$ M$_\odot$) we obtained YSO model fits using the SED fitting program of Robitaille et al. (2007) for those sources with 24 μm photometry. Following Alexander et al. (2012) we use apertures of 2″ for UKIDSS, 3″ for 2MASS and GLIMPSE, and 7″ for MIPSGAL and set a minimum flux uncertainty of 10% to prevent any one data point from dominating the fit. We allowed the distance to vary between 4.3 and 4.7 kpc and A_V to vary between 5 and 50 magnitudes. In Table 3 we show the details of the best-fitting YSO model as well as the YSO stage, where Stage I has $\dot{M}_e/M_* > 10^{-6}$ yr^{-1}, Stage II has $\dot{M}_e/M_* < 10^{-6}$ yr^{-1} and $M_d/M_* > 10^{-6}$ and Stage III has $\dot{M}_e/M_* < 10^{-6}$ yr^{-1} and $M_d/M_* < 10^{-6}$ ($\dot{M}_e$ is the envelope accretion rate in $M_\odot$ yr^{-1}, M_* and M_d are the stellar and disk masses respectively in $M_\odot$), and the

stages typically correspond one-to-one with the observationally defined Class I, II, and III.

The SED fitter typically returned multiple models that were equally good fits statistically. As outlined in Alexander et al. (2012) there are techniques that can be used to obtain a weighted average model for the YSO based on this redundancy. In this paper, since we are using the SED fitter primarily to compare with CC diagram classifications and as a rough check on the YSO mass, we simply report the details of the single best-fitting model. We find that our best-fit models are all in the intermediate-mass range $\sim 2-10$ $M_{\odot}$.

A comparison between the SED fitting results and the results from the Rho et al. (2006) CC diagram is interesting. Sources G18-1, G18-2, G19-3, and G19-7 all lie well within the Class I region of the CC diagram and are also identified as Stage I objects by the SED fitter. All but one of the YSOs with [3.6]-[5.8] between 1.5 and 2.5, including the two "hot excess" sources, are classified as reddened Stage II objects by the SED fitter. The exception is the reddest source, G19-17 which is classified as Stage I. For the sources with [3.6]-[5.8]<1 agreement between the CC diagram and the SED fitter is mixed; the SED fitter classifies G19-6 as Stage II, but classifies G18-9 as Stage III and the very red G19-8 YSO as Stage I.

6. Conclusions

This study represents the first study of W 39 at high resolution at infrared and radio wavelengths. The main conclusions of our study are:

1) W 39 is a giant H II region powered by numerous OB stars with a likely total ionizing luminosity $\log(Q) > 50$, roughly equivalent to a cluster of over 30 O8 V stars. Future work will focus on identifying the OB stars powering W 39, using techniques described in Alexander et al. (2012), as the first step toward obtaining a non-kinematic

distance estimate to the region.

2) Three compact H II regions are located on the periphery of W 39. These regions are each likely powered by a single late O-type star (O7 - O9 V). Two of the regions have a distinct dust-filled bubble morphology seen in infrared 8.0 and 24 μm images.

3) Simple kinematic models suggest that the Myr timescales associated with the expansion of W 39 are about an order of magnitude larger than the evolutionary timescales associated with the smaller H II regions. This is consistent with the scenario where the formation of the smaller H II regions is triggered by the expansion of W 39.

4) Recent star formation surrounding W 39 is not restricted just to the massive stars powering the the small H II regions. We used infrared data to identify a number of young/heavily-embedded intermediate-mass YSOs not directly associated with the H II regions.

5) Star formation activity is not distributed uniformly around the periphery of W 39, rather it is concentrated in the two regions surrounding the small H II regions and potentially in an IRDC that may be associated with the front or rear wall of a bubble structure. Future studies of the W 39 region will explore the stellar content of the compact H II regions in more detail, and will examine the potential relationship of the IRDC with W 39.

This work is partially supported through NASA grant ADAP-NNX10AD55G. The authors would like to thank Massimo Marengo for sharing the *Spitzer* AGB data and Chip Kobulnicky for his helpful comments and suggestions regarding YSO identification.

Facilities: Spitzer, 2MASS, UKIRT, CSO, VLA, FCRAO

REFERENCES

Alexander, M.J., Kobulnicky, H.A., Arvidsson, K., & Kerton, C.R. 2012, ApJ, submitted

Allen, L.E., Calvet, N., D'Alessio, P. et al. 2004, ApJS, 154, 363

Arvidsson, K. & Kerton, C. R. 2011, AJ, 141, 153

Benjamin R. A., Churchwell, E., Babler, B. L., et al. 2003, PASP, 115, 953

Brogan, C.L., Gelfand, J.D., Gaensler, B.M., Kassim, N.E., & Lazio, T.J.W. 2006, ApJ, 639, 25

Carery, S.J., Noriega-Crespo, A., Mizuno, D.R., et al. 2009, PASP, 121, 76

Churchwell, E. 1975, in Lecture Notes in Physics 42, HII Regions and Related Topics, ed. T.L. Wilson & D. Downes, (New York: Springer-Verlag), page

Churchwell, E., Povich, M.S., Allen, D. et al. 2006, ApJ, 649, 759

Churchwell, E., Babler, B.L., Meade, M.R., et al. 2009, PASP, 121, 213

Clemens, D.P. 1985, ApJ, 295, 422

Conti, P.S. & Crowther, P.A. 2004, MNRAS, 355, 899

Crowther, P.A. 2005, in IAU Symp. 227, Massive Star Birth: A Crossroads of Astrophysics, ed. R. Cesaroni, M. Felli, E. Churchwell, & C.M. Walmsley, (Cambridge: Cambridge University Press), 389.

Emerson, J.P. 1988, in NATO ASIC Proc. 241, Formation and Evolution of Low Mass Stars, ed. A.K. Dupree & M.T.V.T. Lago (Dordrecht: Kluwer), 193

Engelbracht, C.W., Blaylock, M., Su, K.Y.L., et al. 2007, PASP, 119, 994

Finkenzeller, U. & Mundt, R. 1984, A&AS, 55, 109

Giard, M., Bernard, J.P., Lacombe, F., Normand, P., & Rouan, D. 1994, A&A, 289, 524

Hartmann, L., Megeath, S.T., Allen, L. et al. 2005, ApJ, 629, 881

Helfand, D. J., Becker, R. H., White, R. L., Fallon, A., & Tuttle, S. 2006, AJ, 131, 2525

Higgs, L.A., Hoffmann, A.P., & Willis, A.G. 1997, in ASP Conf. Ser. 125, Astronomical Data Analsis Software and Systems VI, ed. G. Hunt & H.E. Payne (San Francisco, CA: ASP), 58.

Jackson, J. M., Rathborne, J. M., Shah, R. Y., et al. 2006, ApJS, 163, 145

Johanson, A.K. & Kerton, C.R. 2009, AJ, 138, 1615

Kerton, C.R., Ballantyne, D.R., & Martin, P.G. 1999, AJ, 117, 2485

Kerton, C.R., Arvidsson, K., Knee, L.B.G., & Brunt, C. 2008, MNRAS, 385, 995

Kauffmann, J., Bertoldi, F., Bourke, T.L., Evans, N.J., & Lee, C.W. 2008, A&A, 487, 993

Lockman, F. J. 1989, ApJS, 71, 469

Lucas, P.W., Hoare, M.G., Longmore, A., et al. 2008, MNRAS, 391, 136

Matsakis, D.N., Evans, N.J., Sato, T., & Zuckerman, B. 1976, AJ, 81, 172

Megeath, S.T., Allen, L.E., Gutermuth, R.A., et al. 2004, ApJS, 154, 367

Mezger, P.G. & Henderson, A.P. 1967, ApJ, 147, 471

Osterbrock, D.E. 1989, Astrophysics of Gaseous Nebulae and Active Galactic Nuclei (Sausalito, CA: University Science Books)

Pohl, M., Englmaier, P., & Bissantz, N. 2008, ApJ, 677, 283

Rho, J., Reach, W.T., Lefloch, B., & Fazio, G.G. 2006, ApJ, 643, 965

Robitaille, T.P., Whitney, B.A., Indebetouw, R., & Wood, K. 2007, ApJS, 169, 328

Rosolowsky, E., Dunham, M. K., Ginsburg, A., et al. 2010, ApJS, 188, 123

Rubin, R. H. 1968, ApJ, 154, 391

Russeil, D. 2003, A&A, 397, 133

Schaerer, D. & de Koter, A. 1997, A&A, 322, 598

Simpson, R. J., Povich, M. S., Kendrew, S., et al. 2012, MNRAS, 424, 2442

Skrutskie, M.F., Cutri, R.M., Stiening, R., et al. 2006, AJ, 131, 1163

Spitzer, L. 1978, Physical Processes in the Interstellar Medium (New York: John Wiley & Sons)

Stil, J. M., Taylor, A. R., Dickey, J. M., et al. 2006, AJ, 132, 1158

The, P.S., de Winter, D., & Perez, M.R. 1994, A&AS, 104, 315

Tielens, A.G.G.M., Meixner, M.M., van der Werf, P.P., et al. 1993, Science, 262, 86

Ward-Thompson, D. 2002, Science, 295, 76

Westerhout, G. 1958, BAN, 14, 215

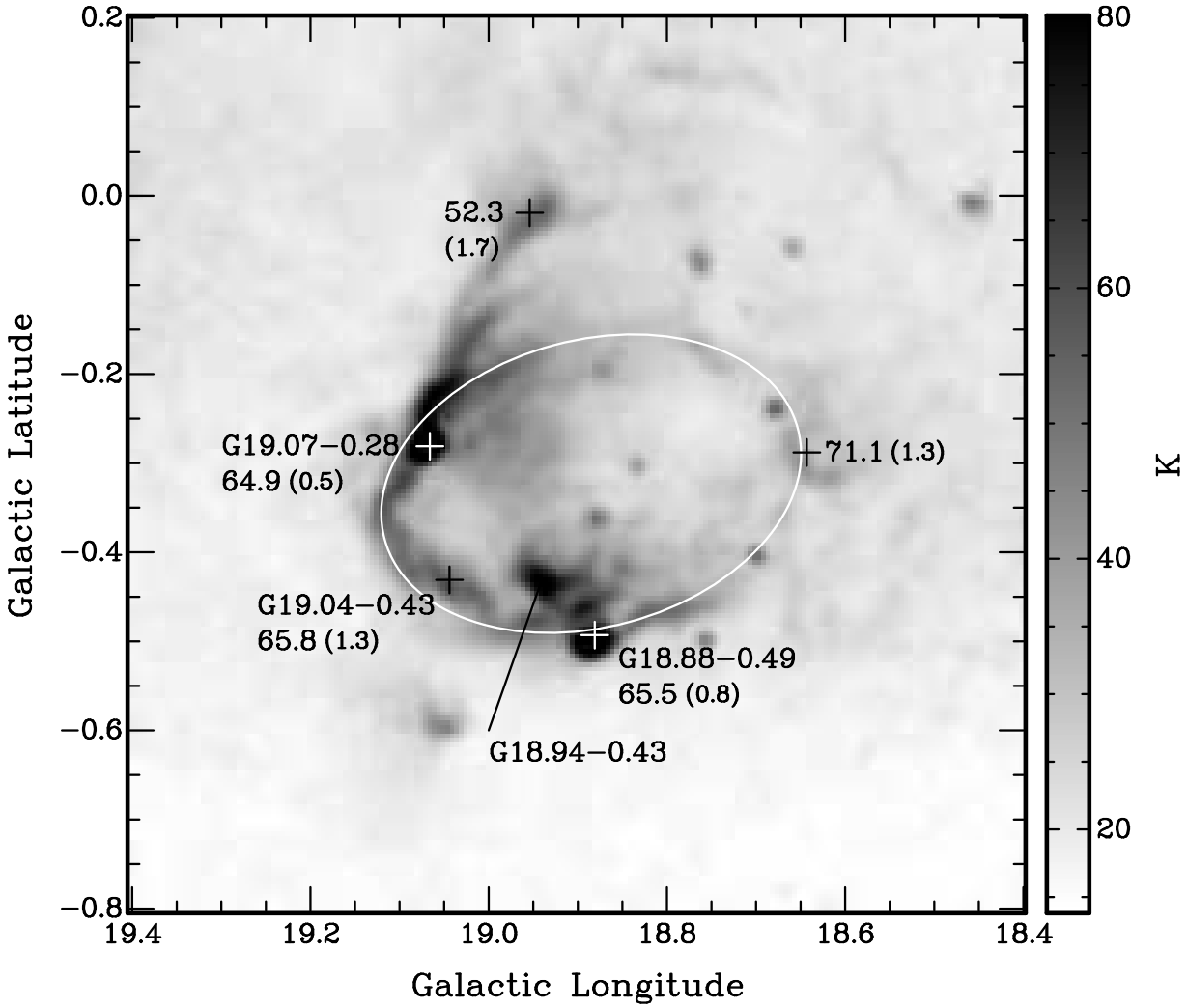

Fig. 1.— VGPS 1420 MHz continuum image of the W 39 region. Crosses indicate the positions of RRL observations from Lockman (1989). The peak velocity ($V_{\rm LSR}$, km s^{-1}) of each RRL profile is also shown with the fit uncertainty given in parentheses. The position of the H II region G18.94-0.43 is also shown. The white ellipse approximately traces the position of the bubble structure best seen in the infrared (see Figure 3).

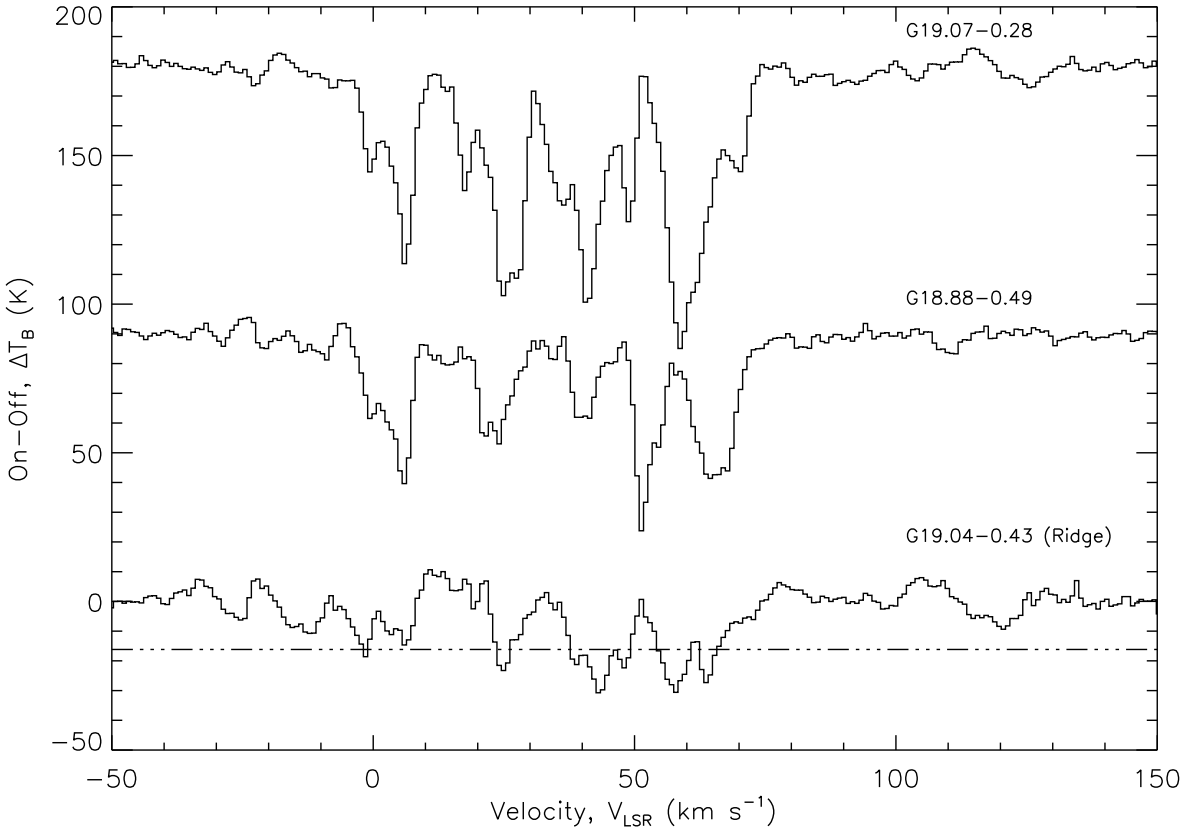

Fig. 2.— H I absorption spectra toward W 39. Spectra of two compact H II regions (G19.07-0.28 and G18.88-0.49) and of a portion of the continuum ridge between the regions (G19.04-0.43) were obtained using data from the VGPS. The G18.88-0.49 and G19.07-0.28 spectra have been offset by 90 K and 180 K for clarity, and the 3σ significance cutoff (dash-dot line) is shown for the G19.04 spectrum. At $l \sim 19°$ the model-dependent tangent velocity is 110 to 140 km s^{-1}. Note the lack of any significant absorption signal beyond ~ 65 km s^{-1} in all three cases showing that W 39 is located at the near kinematic distance.

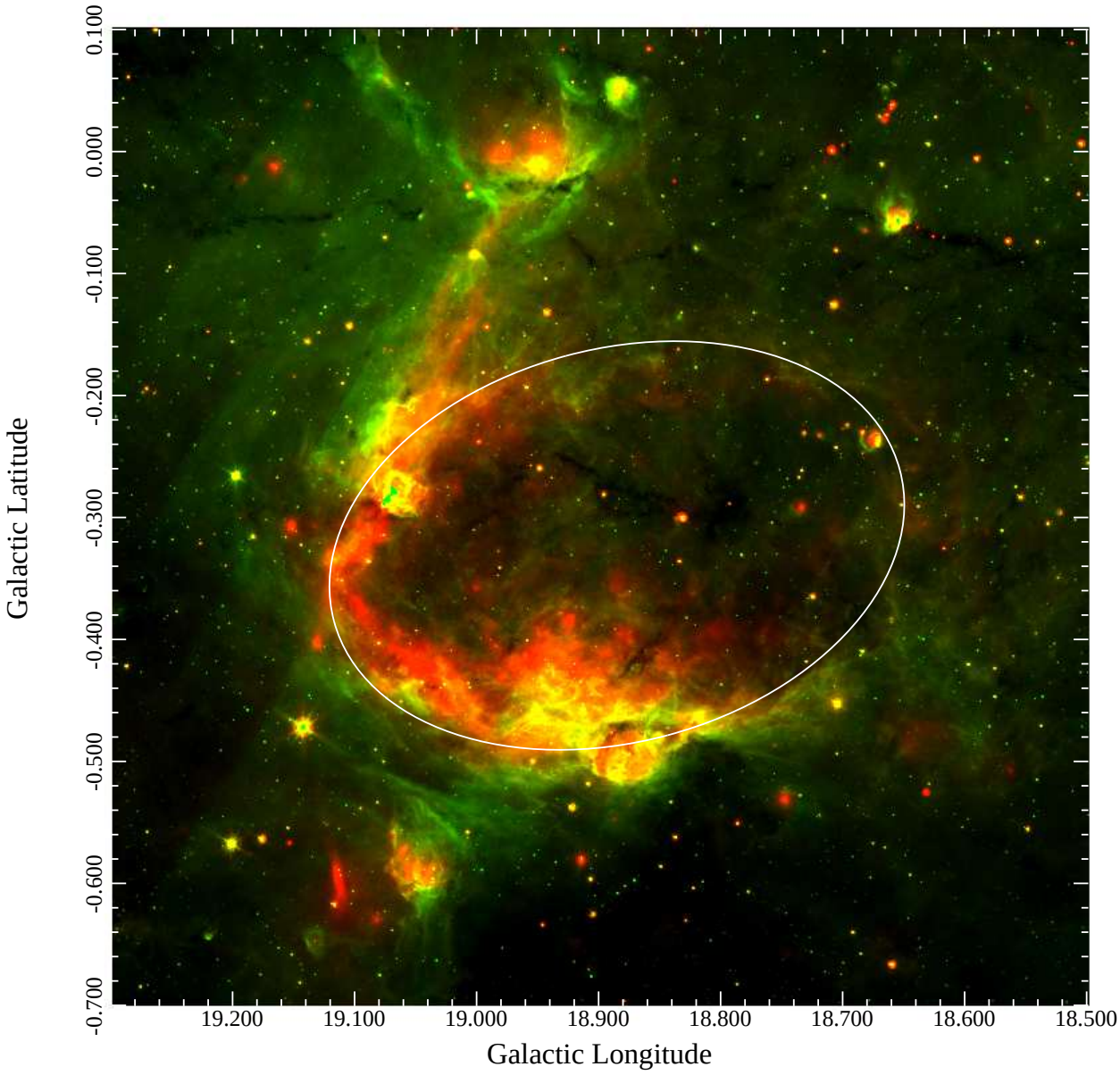

Fig. 3.— GLIMPSE and MIPSGAL image of W 39. This image combines 8 and 24 μm images from the GLIMPSE and MIPSGAL surveys (green and red respectively). The hierarchical bubble structure of W 39, consisting of the main bubble (white ellipse) and the two compact H II regions G18.88-0.49 and G19.07-0.28, is best seen at 8.0 μm. As discussed in the text, the relative position of the 24 and 8 μm emission is consistent with W 39 being a single large H II region. The white ellipse is the same as that shown in Figure 1.

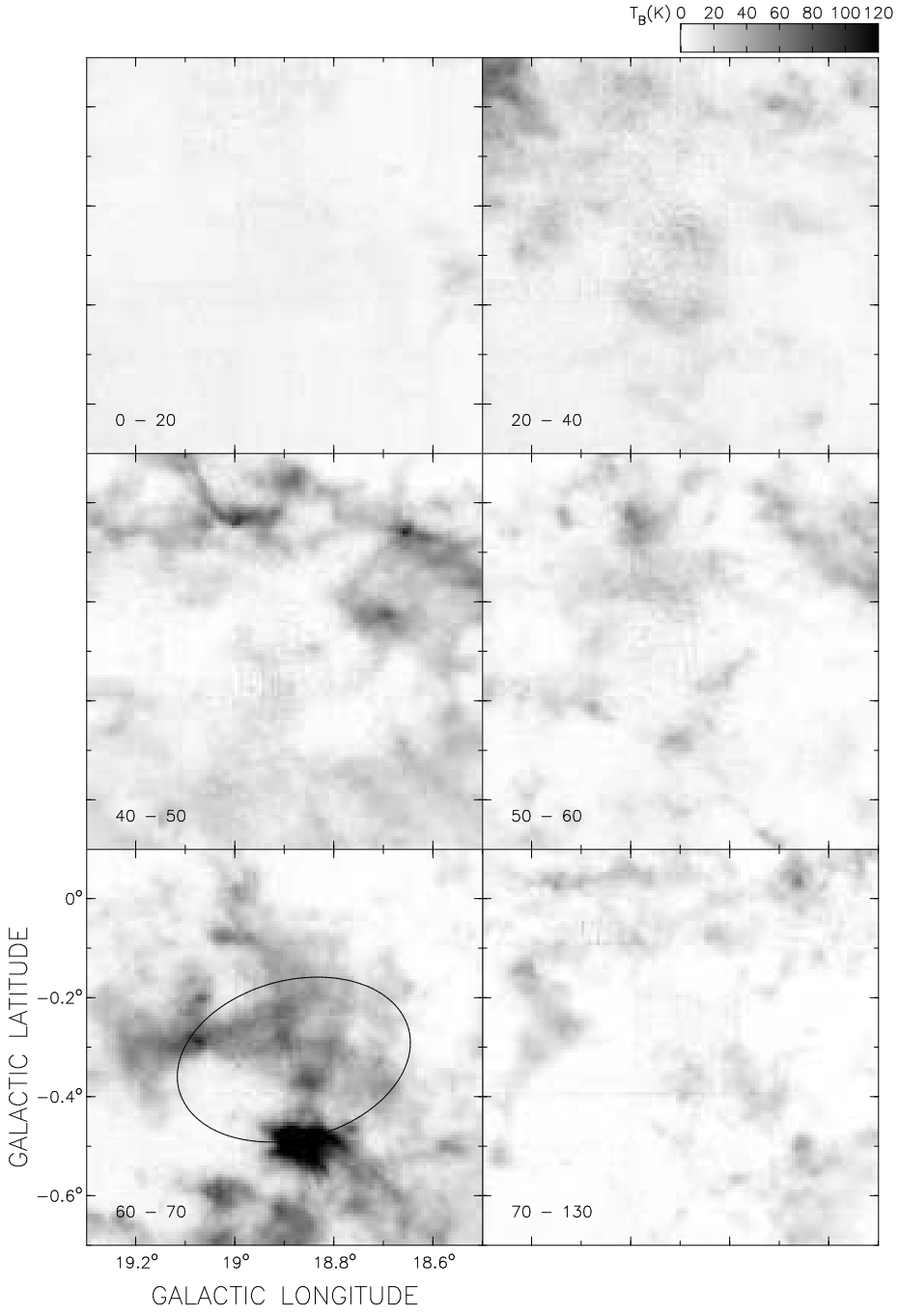

Fig. 4.— Integrated ^{13}CO GRS images between $0 \leq V_{\rm LSR} \leq +130$ km s^{-1}. The velocity increments are shown in the lower-left corner of each panel, and the greyscale is the same in all panels. Note the similarity of the emission seen at high latitude in the $40 - 50$ km s^{-1} panel and the IRDCs seen in Figure 3, and the concentration of material associated with the two main regions of star formation around W 39 shown in the $60 - 70$ km s^{-1} panel. The ellipse is the same as that shown in Figure 1.

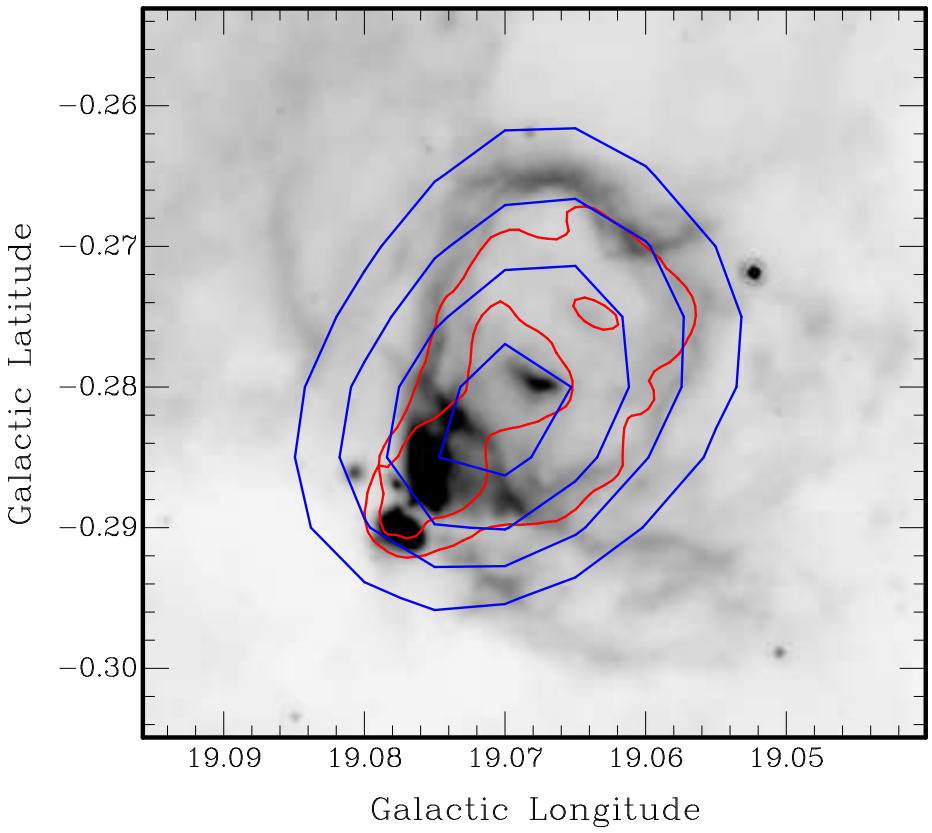

Fig. 5.— The G19.07-0.28 H II region. The bubble structure of this H II region is clearly shown in the GLIMPSE 8.0 μm image. The red (or lighter) contour (at 950 MJy sr^{-1}) traces 24 μm emission from hot dust filling the interior of the bubble. The 24 μm emission is saturated in the MIPSGAL image within the innermost contour shown. Radio continuum emission at 1420 MHz from the VGPS (blue/darker contours; 100 to 175 K at 25 K intervals) also peaks within the infrared bubble.

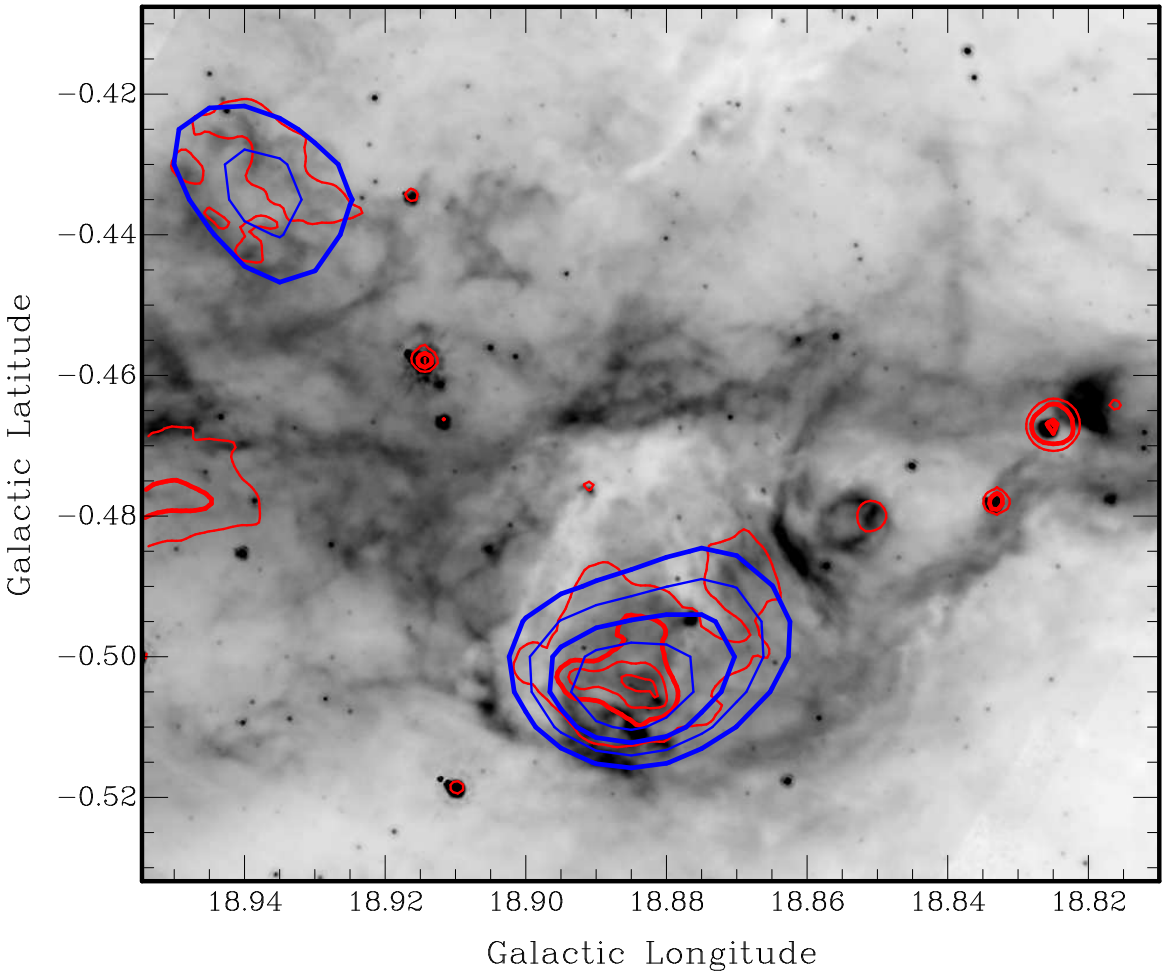

Fig. 6.— The H II regions G18.88-0.49 and G18.94-0.43. This GLIMPSE 8.0 μm image shows two of the compact H II regions surrounding W 39. Red (or lighter) contours (at 550, 1000, and 1550 MJy sr^{-1}) trace MIPSGAL 24 μm emission, and blue (or darker) contours trace 1420 MHz radio continuum emission (80 to 110 at 10 K intervals). Note that the MIPSGAL image is saturated at the center of the G18.88-0.49 H II region.

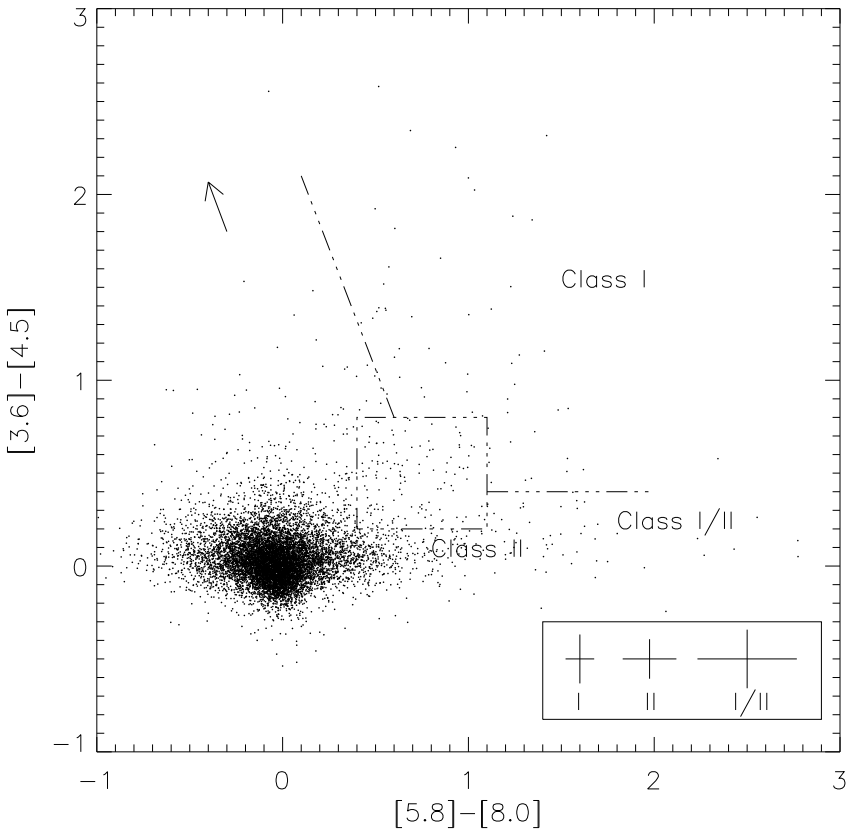

Fig. 7.— GLIMPSE Color-Color Diagram. A total of 10657 sources with valid magnitudes in all four IRAC bands and located in the W 39 field (see text) are plotted. The YSO identification criteria from Allen et al. (2004) are shown as dash-dot lines. For clarity only the median color errors are shown for each of the YSO classes. A reddening vector for a YSO with $A_V = 20$ is shown from Megeath et al. (2004).

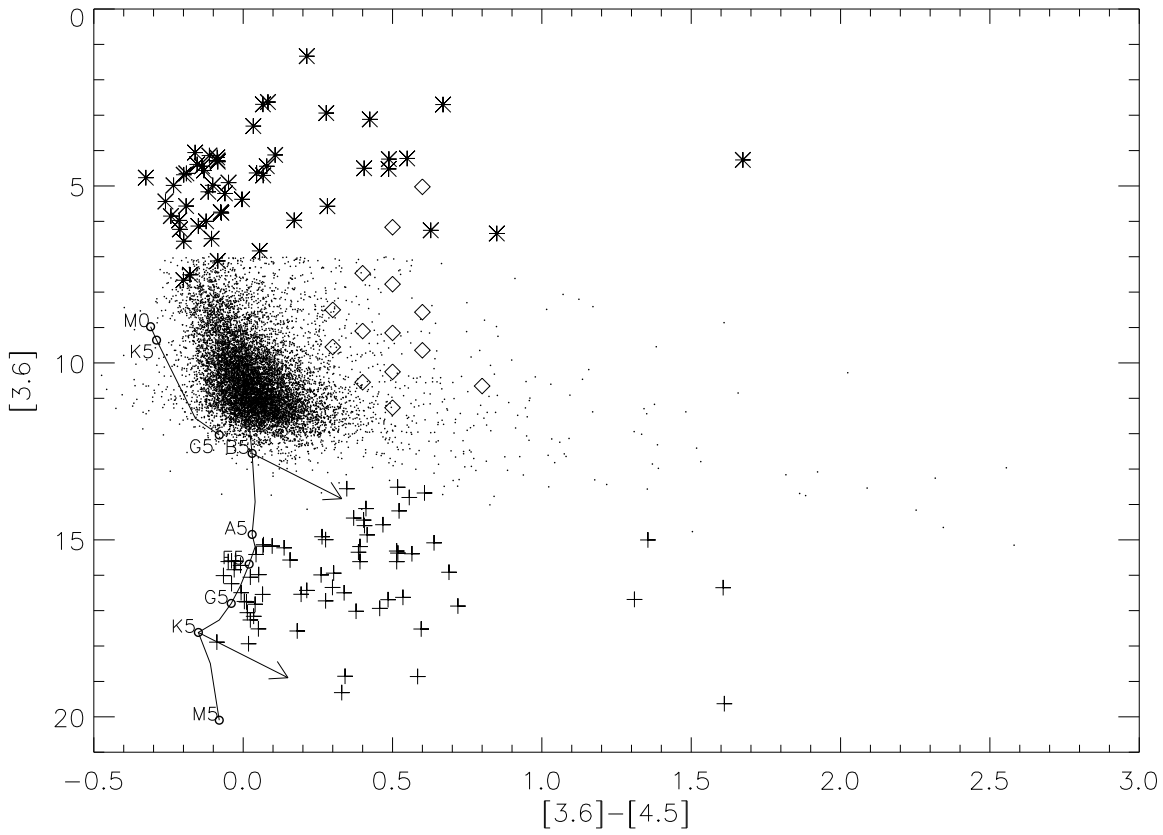

Fig. 8.— GLIMPSE Color-Magnitude Diagram. The sample from Figure 7 is plotted along with a main sequence and giant branch shifted to the distance of W 39. Note the bright limit at ~ 7 due to saturation and a faint, color-dependent, sensitivity cutoff at $[3.6] \sim 13 - 15$. Also shown are representative T Tauri stars (crosses), Herbig AeBe stars (diamonds) and AGB stars (asterisks) also plotted at a distance of 4.5 kpc (see text for details). The CMD shows that, at the distance of W 39, our GLIMPSE sample will be able to detect intermediate-mass YSOs, and that the primary source of confusion for red objects will be background AGB stars.

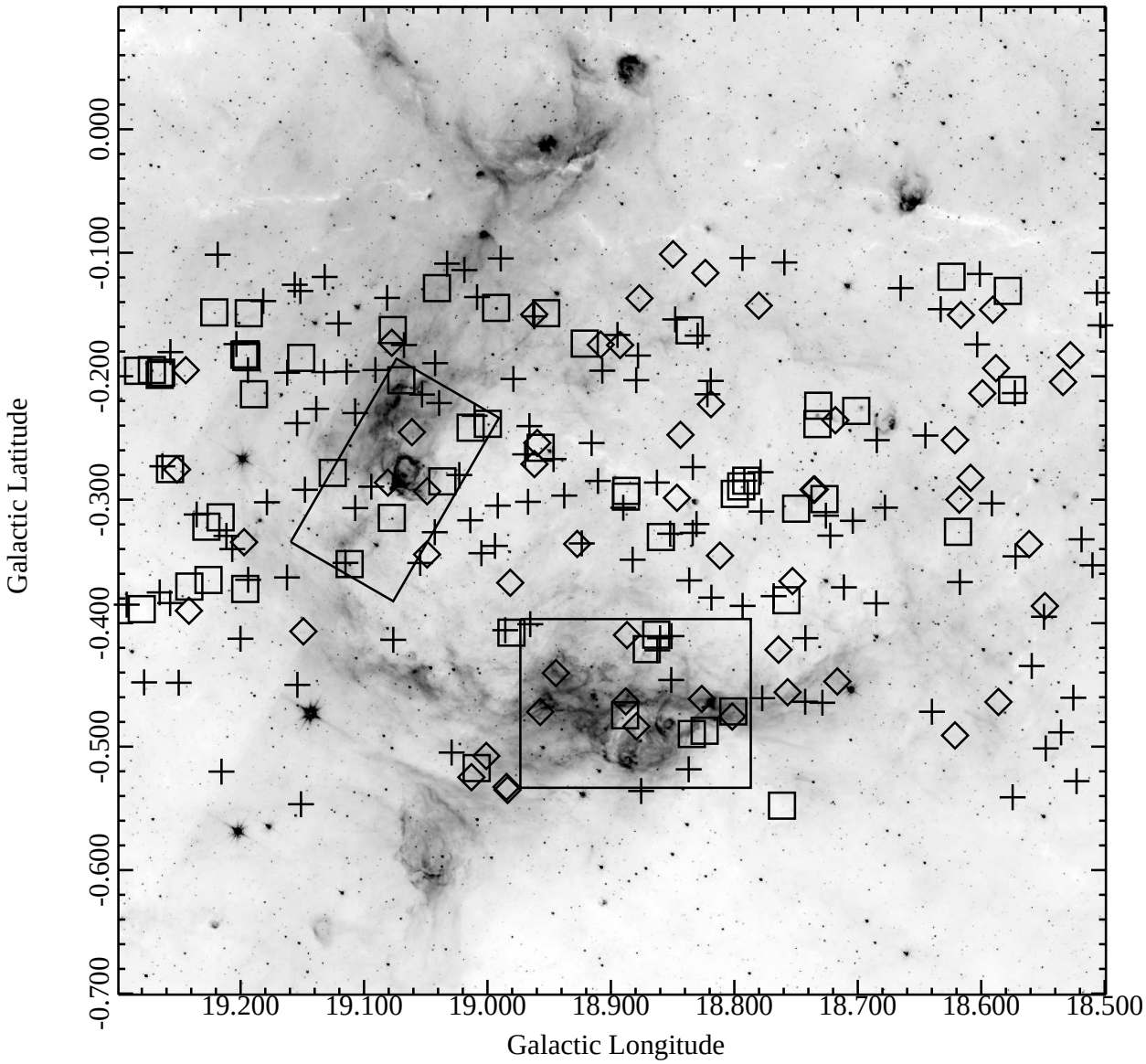

Fig. 9.— W 39 YSO candidates. The location of the various YSO candidates identified using the GLIMPSE CC diagram (Figure 7) are shown: Class I = square, Class II = +, Class I/II = diamond. The rectangles indicate regions around G18.88-0.49 and G19.07-0.28 where the YSO population was investigated in more detail.

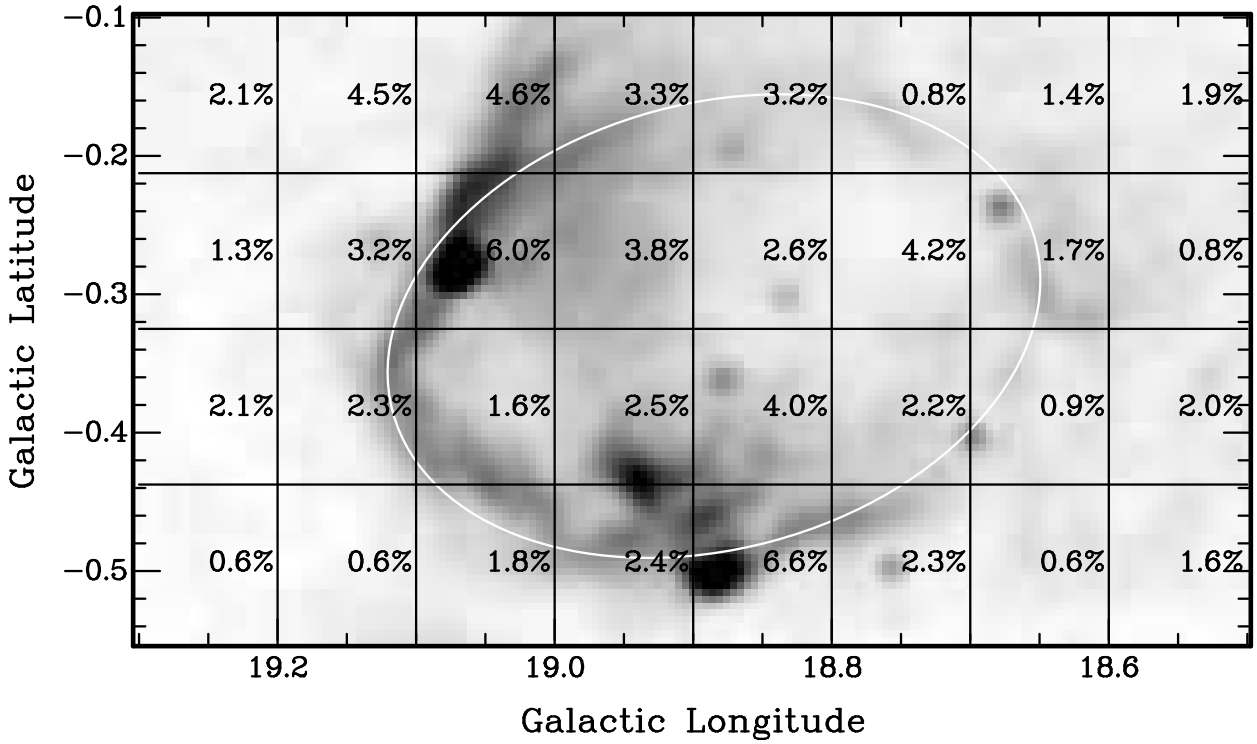

Fig. 10.— YSO Candidate Frequency. The percentage of GLIMPSE sources in each $\sim 0\overset{\circ}{.}1 \times 0\overset{\circ}{.}1$ area classified as YSO candidates is shown. For reference the greyscale shows VGPS 1420 MHz emission and the white ellipse indicates the extent of the IR bubble. Note that the regions around G18.88-0.49 and G19.07-0.28 have the highest YSO percentage in the field and stand well above the median background value of 1.8%, which was defined using the eight high and low longitude areas.

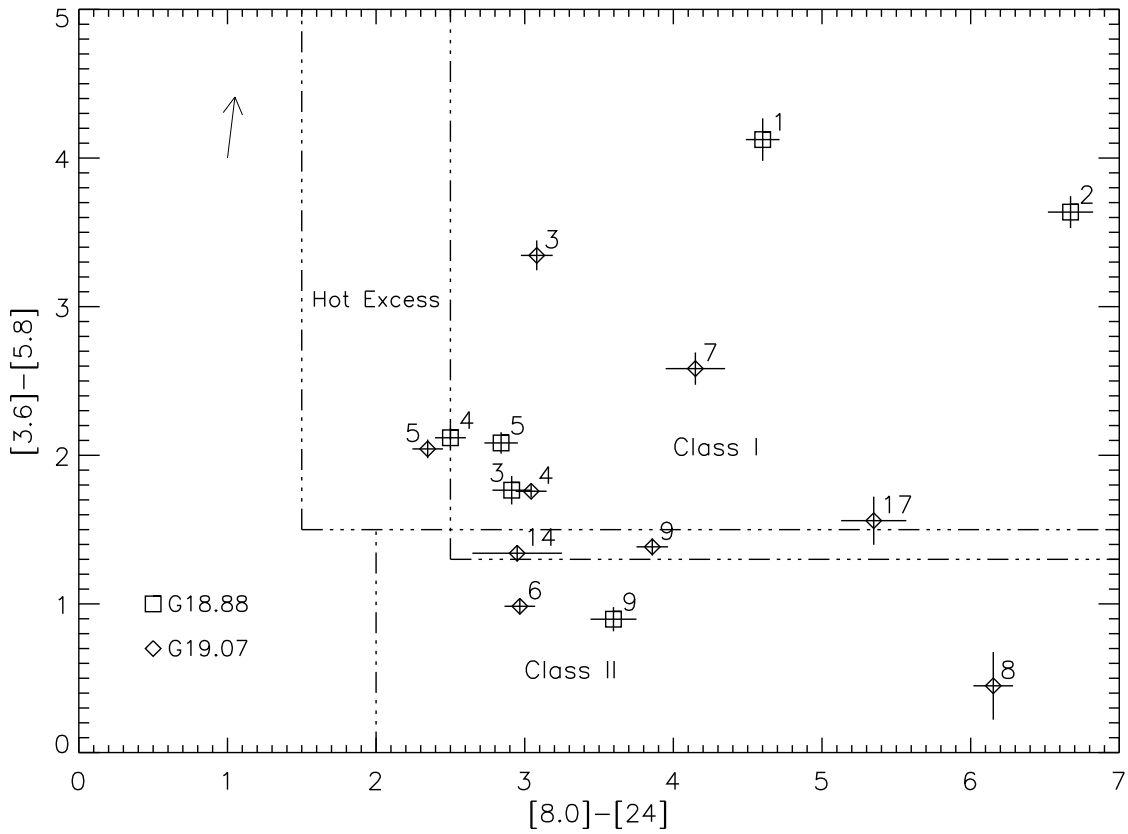

Fig. 11.— GLIMPSE and MIPSGAL Color-Color Diagram. YSOs in the G18.88-0.49 and G19.07-0.28 regions (the rectangles in Figure 9) with 24 μm photometry are plotted along with the YSO classification criteria of Rho et al. (2006). A reddening vector for $A_V = 20$ from Rho et al. (2006) is shown.

Table 1. Photometry for YSO Candidates in the G18.88 and G19.07 Regions

ID	SSTGLMC	J	H	K_s	[3.6]	[4.5]	[5.8]	[8.0]	[24]
G18-1	G018.8008-00.4714	18.621(0.073)	16.716(0.028)	15.152(0.018)	13.256(0.134)	10.939(0.044)	9.132(0.050)	7.711(0.053)	3.11(0.1)
G18-2	G018.8885-00.4746	17.940(0.04)	16.828(0.035)	14.651(0.013)	12.963(0.083)	10.408(0.199)	9.327(0.068)	9.402(0.115)	2.73(0.1)
G18-3	G018.8709-00.4210	17.628(0.03)	15.308(0.009)	13.312(0.004)	10.994(0.071)	10.034(0.068)	9.229(0.064)	8.482(0.082)	5.57(0.1)
G18-4	G018.8240-00.4871	···	···	14.615(0.011)	11.293(0.049)	9.951(0.054)	9.175(0.047)	8.480(0.028)	5.98(0.1)
G18-5	G018.8632-00.4093	···	···	13.420(0.004)	10.911(0.058)	9.817(0.054)	8.828(0.043)	7.951(0.052)	5.11(0.1)
G18-6	G018.8344-00.4897	···	···	···	13.080(0.146)	11.157(0.090)	9.890(0.101)	9.392(0.179)	···
G18-7	G018.9653-00.4008	···	15.743(0.013)	13.357(0.004)	12.016(0.187)	11.761(0.094)	11.244(0.120)	10.646(0.149)	···
G18-8	G018.8509-00.4104	14.680(0.041)	13.260(0.035)	12.293(0.036)	10.645(0.048)	10.104(0.061)	9.594(0.055)	8.950(0.085)	···
G18-9	G018.8623-00.4220	18.260(0.06)	14.051(0.079)	11.900(0.034)	10.366(0.053)	10.160(0.044)	9.469(0.062)	8.657(0.118)	5.06(0.1)
G18-10	G018.8601-00.4122	···	···	···	11.964(0.066)	11.417(0.094)	10.627(0.089)	9.892(0.137)	···
G18-11	G018.8369-00.5183	···	16.546(0.024)	13.760(0.056)	11.882(0.081)	11.451(0.070)	10.882(0.072)	10.440(0.154)	···
G18-12	G018.8510-00.4460	17.477(0.026)	13.779(0.002)	11.874(0.001)	10.557(0.036)	10.268(0.065)	9.792(0.070)	9.337(0.165)	···
G18-13	G018.8793-00.4835	···	17.544(0.067)	15.021(0.018)	13.201(0.121)	13.101(0.154)	10.617(0.226)	9.372(0.305)	···
G18-14	G018.8879-00.4633	14.138(0.038)	12.501(0.028)	11.897(0.025)	11.399(0.083)	11.408(0.054)	11.528(0.339)	9.581(0.274)	···
G18-15	G018.9445-00.4404	16.538(0.012)	14.426(0.004)	13.203(0.004)	12.248(0.131)	12.187(0.124)	11.402(0.237)	10.203(0.199)	···
G18-16	G018.8869-00.4096	18.539(0.07)	15.156(0.008)	13.589(0.005)	12.613(0.072)	12.436(0.099)	12.080(0.197)	10.820(0.159)	···
G18-17	G018.8263-00.4613	···	17.650(0.07)	14.761(0.01)	12.656(0.117)	12.484(0.169)	10.700(0.139)	9.203(0.223)	···
G18-18	G018.8016-00.4756	13.295(0.033)	12.535(0.033)	12.282(0.039)	12.113(0.079)	12.062(0.065)	11.586(0.334)	8.812(0.250)	···
G18-19	G018.9573-00.4718	···	12.775(0.046)	11.934(0.040)	11.152(0.135)	11.092(0.123)	10.313(0.164)	8.804(0.350)	···
G19-1	G019.0697-00.2032	···	···	14.885(0.015)	12.787(0.135)	12.278(0.155)	10.854(0.300)	9.324(0.141)	···
G19-2	G019.0365-00.2851	···	···	15.916(0.042)	12.937(0.118)	12.195(0.111)	11.342(0.126)	10.236(0.102)	···
G19-3	G019.0136-00.2416	···	···	···	13.536(0.088)	11.447(0.084)	10.191(0.048)	9.191(0.038)	6.11(0.1)
G19-4	G019.1116-00.3521	16.085(0.008)	12.961(0.001)	10.335(0.001)	7.614(0.030)	6.704(0.051)	5.856(0.029)	5.093(0.028)	2.05(0.1)
G19-5	G019.0774-00.3147	···	15.291(0.009)	11.974(0.001)	8.202(0.052)	7.078(0.059)	6.159(0.035)	5.557(0.025)	3.21(0.1)

Table 1—Continued

ID	SSTGLMC	J	H	K_s	[3.6]	[4.5]	[5.8]	[8.0]	[24]
G19-6	G019.1253-00.2782	13.528(0.001)	12.207(0.001)	10.870(0.001)	9.380(0.039)	8.908(0.047)	8.396(0.038)	7.057(0.025)	4.09(0.1)
G19-7	G018.9996-00.2385	···	13.627(0.036)	11.308(0.046)	8.863(0.090)	7.253(0.102)	6.280(0.061)	5.708(0.173)	1.56(0.1)
G19-8	G019.0391-00.2217	15.994(0.007)	13.901(0.003)	12.665(0.002)	11.909(0.061)	11.638(0.080)	11.460(0.219)	10.402(0.088)	4.25(0.1)
G19-9	G019.0530-00.2148	15.734(0.006)	13.040(0.001)	10.950(0.001)	9.115(0.039)	8.367(0.095)	7.731(0.043)	6.798(0.036)	2.94(0.1)
G19-10	G019.0103-00.2320	17.523(0.027)	14.303(0.004)	12.552(0.002)	11.372(0.056)	11.070(0.073)	10.586(0.114)	10.047(0.150)	···
G19-11	G019.1071-00.3067	···	14.602(0.005)	12.529(0.002)	11.250(0.087)	10.965(0.098)	10.803(0.094)	10.327(0.075)	···
G19-12	G019.0941-00.2894	16.036(0.008)	13.720(0.002)	12.085(0.002)	10.382(0.034)	9.651(0.045)	9.012(0.045)	8.423(0.076)	···
G19-13	G019.0228-00.2800	···	14.449(0.004)	12.779(0.003)	11.545(0.064)	11.302(0.090)	11.188(0.129)	10.597(0.249)	···
G19-14	G019.1150-00.3511	14.682(0.003)	11.561(0.001)	9.568(0.001)	7.371(0.044)	6.846(0.041)	6.030(0.031)	5.449(0.026)	2.5(0.3)
G19-15	G019.0488-00.2932	13.602(0.001)	12.428(0.001)	11.863(0.001)	11.381(0.068)	11.312(0.089)	10.571(0.125)	9.346(0.140)	···
G19-16	G019.0806-00.2861	17.782(0.04)	15.623(0.01)	14.229(0.009)	11.043(0.121)	11.270(0.184)	8.043(0.113)	6.651(0.286)	···
G19-17	G019.0612-00.2453	15.077(0.004)	13.922(0.003)	13.219(0.004)	12.274(0.083)	11.964(0.123)	10.714(0.139)	9.128(0.195)	3.78(0.1)

Note. — JHK photometry is from 2MASS for Sources G18-8, G18-9 (H,K), G18-11(K), G18-14, G18-18, G18-19, G19-7, and from UKIDSS-GPS for others.

Table 2. YSO Classification

ID	IRAC Colors [3.6]-[4.5] vs. [5.8]-[8.0]	IRAC & MIPS Colors [3.6]-[5.8] vs. [8.0]-[24]	SED Fitting
G18-1	I	I	I
G18-2	I	I	I
G18-3	I	I	II
G18-4	I	I/HE	II
G18-5	I	I	II
G18-6	I	...	...
G18-7	II	...	...
G18-8	II	...	...
G18-9	II	II	III
G18-10	II	...	...
G18-11	II	...	...
G18-12	II	...	...
G18-13	I/II	...	...
G18-14	I/II	...	...
G18-15	I/II	...	...
G18-16	I/II	...	...
G18-17	I/II	...	...
G18-18	I/II	...	...
G18-19	I/II	...	...
G19-1	I	...	...
G19-2	I	...	...
G19-3	I	I	I
G19-4	I	I	II
G19-5	I	HE	II
G19-6	I	II	II
G19-7	I	I	I
G19-8	II	II	I
G19-9	II	I/II	II
G19-10	II	...	...
G19-11	II	...	...
G19-12	II	...	...

Table 2—Continued

ID	IRAC Colors [3.6]-[4.5] vs. [5.8]-[8.0]	IRAC & MIPS Colors [3.6]-[5.8] vs. [8.0]-[24]	SED Fitting
G19-13	II	···	···
G19-14	II	I/II	II
G19-15	I/II	···	···
G19-16	I/II	···	···
G19-17	I/II	I/II	I

Note. — HE = Hot Excess (Rho et al. 2006); I/II = red sources outside of Class I or II areas for IRAC colors or objects in I/II overlap region for IRAC & MIPS colors; SED fitting done only for sources with [24] data.

Table 3. SED Best-Fit YSO Models for IRAC-MIPS Sources

ID	Model #	Inclination Angle (°)	A_V (mag.)	Stellar Mass M_* ($M_\odot$)	Envelope Accretion Rate $\dot{M}_e$ ($M_\odot$ yr^{-1})	Disk Mass M_d ($M_\odot$)	YSO Stage
G18-1	3008766	18.19	14.52	3.16	8.25×10^{-5}	7.50×10^{-2}	I
G18-2	3009923	49.46	12.28	7.72	4.59×10^{-4}	1.89×10^{-1}	I
G18-3	3002489	81.37	9.75	4.15	0	6.65×10^{-4}	II
G18-4	3012453	81.37	45.36	5.77	0	1.03×10^{-2}	II
G18-5	3014480	81.37	8.89	4.39	0	5.68×10^{-3}	II
G18-9	3003037	49.46	22.31	6.90	0	2.98×10^{-8}	III
G19-3	3012136	18.19	13.20	3.41	1.27×10^{-3}	1.41×10^{-2}	I
G19-4	3002683	81.37	12.81	4.37	0	3.66×10^{-3}	II
G19-5	3014289	75.52	28.43	7.65	0	1.04×10^{-1}	II
G19-6	3018962	18.19	5.11	4.55	0	1.39×10^{-3}	II
G19-7	3010932	18.19	14.35	7.51	4.38×10^{-4}	7.37×10^{-3}	I
G19-8	3008529	41.41	6.19	2.66	3.26×10^{-5}	9.28×10^{-2}	I
G19-9	3015777	41.41	16.34	4.93	9.86×10^{-7}	4.52×10^{-2}	II
G19-14	3017501	75.52	16.34	8.84	0	3.09×10^{-2}	II
G19-17	3013269	18.19	5.34	2.14	3.13×10^{-4}	5.09×10^{-3}	I